HHS Public Access

Author manuscript

Phys Rev Appl. Author manuscript; available in PMC 2023 March 17.

Published in final edited form as:

Phys Rev Appl. 2017 June ; 7(6): . doi:10.1103/physrevapplied.7.064024.

Concentration-Gradient Stabilization with Segregated Counter- and Co-Ion Paths: A Quasistationary Depletion Front for Robust Molecular Isolation or Concentration

Gongchen Sun,

Zehao Pan,

Satyajyoti Senapati,

Hsueh-Chia Chang*

Department of Chemical and Biomolecular Engineering, University of Notre Dame, Notre Dame, Indiana 46556, USA

Abstract

We study the spatiotemporal dynamics of a microfluidic system with a nonselective microfluidic channel gated by an ion-selective membrane which separates the ion flux paths of cations and anions. To preserve electroneutrality, the ionic concentration in the system is shown to converge to a specific inhomogeneous distribution with robust constant current fluxes. A circuit scaling theory that collapses measured asymptotic currents verifies that this is a generic and robust mechanism insensitive to channel geometry, ion selectivity, and electrolyte ionic strength. This first temporally stationary but spatially inhomogeneous depletion front can be used for modulating ionic current and for isotachophoretic isolation of low-mobility molecules and exosomes on small diagnostic chips for various medical applications that require robust high-throughput and integrated platforms.

I. INTRODUCTION

The spatiotemporal dynamics of ions and currents in a microfluidic system with adjoining ion-selective media has long been suspected to be driven by the electroneutrality constraint. Without electric-field or current penetration through the channel walls or the ion-selective media, the field lines and the current lines within a system are identical [1]. Both cations and anions share the same flux lines, though in opposite directions. The net tangential cation and anion fluxes remain the same at every position along the field line and cancel each other out. This flux invariance condition can be specified by the same local tangential electric field along the field or current lines with a spatially homogeneous electrolyte concentration field [1]. Thus, electroneutrality can be preserved without spatial inhomogeneity. However, if an ion-selective membrane separates the flux lines of different ions, or if there is field leakage through the wall [2], the field lines separate from the current lines, which then segregate into two distinct cation and anion flux lines. Under this condition, flux invariance along different field lines cannot be achieved for both ions if the system remains spatially homogeneous.

*Corresponding author. hchang@nd.edu.

Hence, electroneutrality necessarily requires spatial inhomogeneity for such systems with ion-selective media. In his seminal monograph, Rubinstein [3] shows that a diffusion layer with a nonuniform ionic strength appears on one side of an ion-selective membrane under a voltage bias to preserve electro neutrality. A recent analysis by Yariv and Almog [4] (which generalizes the analysis of Ben and Chang [5] of the diffusive current towards the ion-selective membrane) attributes a memory effect in the ion-concentration-polarization dynamics to electroneutrality.

On the other hand, spatially inhomogeneous ion concentration polarization is used in many existing biomedical applications and has been suggested for future ones. Examples in current biotechnology include isoelectric focusing, isotachophoresis, and field-flow fractionation. Ion current rectification across a conic nanopore was recently attributed to a gradient of the mobile ion concentration along the pore [6]. This phenomenon could lead to artificial biomimetic ion channels for control and quantification of specific ions or molecules [7]. Indeed, microfluidic chips with integrated perm-selective membrane modules have been designed to produce on-chip concentration gradients for the control and analysis of macromolecules, such as the transport, concentration, and identification of protein and nucleic-acid biomarkers for autonomous liquid-biopsy platforms in precision medicine [8]. Low concentrations and mobility of these biomarkers require an on-chip analytical system that can isolate the molecules in a short channel. Recent biosensor work [9] shows that the ionic strength jump across a depletion front generated by an ion-selective membrane can be used for the isotachophoretic isolation of molecules, exosomes, and nanoparticles. A common problem in all of these on-chip depletion-front technologies is that, without the presence of large reservoirs, the on-chip inhomogeneous concentration profile is highly dynamic and unstable. A stationary ionic-strength inhomogeneity (a stationary depletion front) that does not require pairing of electrolytes with different salts or pH can produce robust isotachophoretic and isoelectric purification and isolation platforms for low-mobility analytes in a short channel or biochip.

This concentration depletion front is governed by the diffusion equation and can propagate to infinity (or the end of the channel) without reaching a steady state [10]. Current work focuses on using a counter bulk flow, such as an electro-osmotic flow or convective mixing [9,11–15], to balance the advance of the depletion front. However, the counter bulk flow will likely weaken the necessary inhomogeneity and cause dispersion of the analyte. Meanwhile, most counter-bulk-flow methods, such as those using an electro-osmotic flow, are effective only in shallow microchannels (a few micrometers) and cannot allow high-throughput processing of multiple samples in many medical applications.

In this paper, we report a particular coupled-gating geometry between two different ionic paths in a microfluidic chip that can drive the depletion front from an ion-selective membrane to a quasistationary position by using only the eletroneutrality constraint and without introducing a counter bulk flow. The spatial inhomogeneity of the ion concentration in the microchannel stays stable when the transmembrane potential drop and current vanish. This strategy of establishing a quasistationary depletion front can potentially be used to design on-chip isotachophoretic and isoelectric sample-pretreatment modules in integrated medical diagnostic platforms.

II. FABRICATION AND EXPERIMENTAL METHODS

Our system with two different ionic paths consists of a nonselective microfluidic channel that allows both cation and anion electromigration fluxes and an anion-exchange membrane (AEM) that allows only counterion (anion) fluxes. These two ionic paths, one ion selective and one nonselective, intersect perpendicularly, as illustrated in Fig. 1(a), and the fluxes are driven by three electrodes: a gating electrode G outside the membrane and a drain-source (D-S) pair in the cross-channel. These two ionic paths share a common section within the microfluidic channel [Fig. 1(a)]. As a result of this coupling, the charge flux through the selective AEM can be arrested to preserve electroneutrality if the voltage in the shared section V_{membrane} approaches the gating voltage V_g. Once the charge flux through the membrane is arrested, the depletion front stops propagating at a quasistationary position.

In order to prove that our quasistationary depletion front is robust in different microfluidic systems, we fabricate two kinds of hybrid ionic path devices with different geometrical parameters: an AEM-based polycarbonate (PC) microfluidic chip and an AEM-based polydimethylsiloxane (PDMS) microfluidic chip.

The AEM-based PC microfluidic chip consists of three layers of PC sheets, and microchannels are structured by cutting the middle PC sheet on a plotter (Graphtec Cutting Pro FC7000MK2-60). The openings of microchannels for fluidic connections and membrane attachment are cut on the top PC sheet. These three structured PC sheets are then aligned and thermally bonded together at 170°C for 30 min. Channels with two different dimensions are fabricated: 2 mm wide × 28 mm long × 250 μm high and 1 mm wide × 28 mm long × 250 μm high to study the arrest of the depletion front in different nonselective ionic paths discussed later in this paper. Cut pipette tips with a filter paper at the bottom as buffer reservoirs for electrical connection and Tygon tubings as fluidic inlets and outlets are fixed by an UV curable glue (Acrifix 192) onto their designated places on the top PC sheet. A layer of 1% agarose gel is placed on the bottom of each cut pipette-tip reservoir to prevent possible bubble entry and to suppress electro-osmotic flows during electrical measurements. A 1 × 10 mm AEM strip (Mega a.s., Czech Republic) is cut and embedded in the membrane opening on the top PC sheet to cover the microfluidic channel at the designated position. The last step to complete the device is to fix and seal the membrane strip with the UV curable glue, making the membrane closely attached on top of the microfluidic channel and connecting two separated microchannels: one is used as the nonselective ionic path shown in Fig. 1(a), and the other one to apply gating voltage on the other side of the membrane. The AEM-based PC microfluidic chips are used in experiments shown in Fig. 4.

The AEM-based PDMS microfluidic chip is fabricated using the PDMS casting method against a glass-tape-membrane master of fluidic structures. A layer of double-sided Kapton tape with a 100-μm thickness is cut with the plotter and then transferred onto a precleaned glass substrate as the channel mold. The mold defines a channel with the dimensions 2 mm wide × 28 mm long × 100 μm high as the nonselective ionic path. A 1 × 10 mm AEM strip is fixed onto the double-sided-tape mold at the designated place. Similarly, the membrane strip connects two channels: one channel as the nonselective ionic path and the other one for gating-voltage application. Silicone tubings for both fluidic inlets and outlets and electrical

connections are positioned onto the double-sided-tape mold to complete the casting master. A PDMS prepolymer (Sylgard 184) is prepared by mixing the base and the curing agent in a weight ratio of 10:1 and is degassed in vacuum for 15 min. The PDMS prepolymer is then poured onto the completed master and degassed again. The whole structure is cured in an oven at 70°C or 50 min. The cured PDMS cast is peeled off and bonded onto a precleaned glass slide using corona discharge followed by thermal bonding at 70°C for 2 h to complete the device. Both devices are filled with 10-mM potassium chloride (KCl) solution for 48 h to let the AEM swell properly prior to use. The AEM-based PDMS microfluidic chips are used in experiments shown in Figs. 1–4.

To understand the dynamics of establishing the stationary depletion front, we perform a two-channel chronoamperometry experiment on both microfluidic systems with real-time fluorescence imaging. A 10-mM KCl solution is used as the electrolyte in all electrical characterizations. External voltages are applied through platinum wires on the G, D, and S ends [Fig. 1(a)] of the microfluidic system simultaneously. In each measurement, the transmembrane current I_{membrane} measured from the G end and the cross-channel current I_d measured from the D end are recorded for over 300 s by a Keithley 2636A Dual-Channel System SourceMeter Instrument. The gated and normalized ionic resistance of the cross-channel is subsequently calculated from the steady-state I_d. To visualize the ion-concentration-polarization region, we use 100 μM cationic Rhodamine 6G dye dissolved in a 10-mM KCl solution as a fluorescence indicator without changing the conductivity of the buffer. The visualization process is performed on a customized dark-room platform equipped with a Dark Reader Transilluminator (Clare Chemical) to excite the fluorescent dye from the top of the microfluidic chip. Fluorescence images are taken from the bottom of the microfluidic chip by a QImaging Retiga 2000R Fast 1394 camera synchronized with the Keithley SourceMeter Instrument through a custom MATLAB code.

III. RESULTS AND DISCUSSION

We assign the S end of the cross-channel as the electric-potential reference point (GND) and set a constant negative voltage V_d at the D end of the cross-channel to electrophoretically drive ion fluxes through the nonselective ionic path. By properly applying a negative potential V_g (between GND and V_d) at the G end of the anion-selective path, an ion depletion zone and an ion enrichment zone can be generated simultaneously in the cross-channel [16]. The dynamics towards an electroneutral state, with vanishing transmembrane current [Fig. 2(c)], involve equilibration of the voltage V_{membrane} that is at the junction of the two ionic paths [the shared section in Fig. 1(a)] towards V_g. The adjustment of V_{membrane} during the equilibration results from propagation of the depletion front towards a specific location at the D end of the cross-channel. Unlike a homogeneous electrolyte, which usually produces a linear electric potential profile along the channel, this depletion amplifies the ionic resistance and redistributes the electric potential along the cross-channel until $V_{\text{membrane}} = V_g$.

In the actual device, due to the finite width of the AEM, the local value of V_{membrane} varies slightly along the interface between the membrane and the cross-channel when the depletion front approaches the specific location. Although the net transmembrane current

across the membrane vanishes in the normal direction, such a tangential potential difference of V_{membrane} results in a tangential cross-membrane anion flux which enters the AEM from the left side of the cross-channel and exits to the right side. The established depletion zone to the right (the D side) of the membrane can hence be maintained. However, this tangential cross-membrane anion flux is much smaller than the original transmembrane flux, with far smaller space-charge creation and anion depletion rates. As seen in the fluorescence image inset of Fig. 1(a), simultaneous ion enrichment to the left and depletion to the right occur on the channel side of the gating membrane, supporting the development of a tangential cross-membrane anion flux entering and exiting the finite-width membrane without penetration [17]. This tangential anion flux across the membrane sustains the depletion-front position but not its original front speed.

Figure 1(b) shows the cross-channel current evolution with V_d set at −20 V but with different V_g's ranging from −1 to −2 V. I_d approaches different steady-state values for different V_g's with slight variations at the end of all three experiments, indicating that the depletion front stabilizes and the cross-channel ionic resistance approaches specific values. The slight variation in current is due to a weak vortex instability developed on the depletion side of the membrane. However, by designing the cross-channel wall parallel to the AEM with a small separation (100 μm) [10], we are able to suppress the vortex instability so that it does not arrest the depletion growth and disturb the stabilization of the cross-channel current.

For an unbounded symmetric electrolyte without two segregated current paths, the depletion front from an ion-selective membrane advances rapidly to infinity with a universal self-similar diffusive scaling $\sqrt{Dt}$ [18]. However, the tracking of the instantaneous length of the ion depletion region L_{dep} (by low intensity of the cationic fluorescence indicator) in our system with two different ionic paths (V_g = −2.5 V and V_d = −15 V) indicates that initial diffusive dynamics develop into a slow nondiffusive one [Fig. 2(a)] at the same time when I_d approaches steady state. The fact that the initial depletion-front evolution follows the self-similar diffusive scaling indicates that the hydrodynamic vortex instabilities and convections are suppressed. However, the deviation of depletion growth from the diffusive scaling after 90 s [Fig. 2(b)] suggests that the depletion front ceases to advance rapidly and approaches a stationary position to suppress space-charge creation. The cationic fluorescent dyes can only migrate linearly with a limited electrophoretic mobility, when they enter the homogeneous low-electric-field region beyond the quasistationary depletion front after t = 90 s. The arrested concentration polarization region is about 20 mm away from the D end of the channel, far from the end boundary. The movie which shows the real-time growth and arrest of the depletion front can be found in the Supplemental Material [19]. Owing to the negative surface charges of the PDMS microchannel [20], electro-osmotic flow may be generated at the cross-channel during the growth of the depletion front. In order to suppress net electro-osmotic convection, we seal the end tubings for electric connections at both the S end and the D end of the cross-channel by glue [10]. The closed microchannel encapsulates the electrolyte and hence suppresses net electro-osmotic convections or amplified electrokinetic flows [21]. A pair of vortices due to a weak backflow from the D end can still be observed in Fig. 2(a) and causes small fluctuations in the

cross-channel current [Fig. 2(c)]. We can further eliminate the electro-osmotic instability by chemically modifying the PDMS microchannels to remove surface charges [22], or by filling the microchannel with hydrogels to block the flow [9].

The currents through these two ionic paths during the process of the depletion-region evolution are measured simultaneously [shown in Fig. 2(c)]. As a result of the negative feedback from the depletion growth, V_{membrane} approaching V_g renders the current flowing through the AEM anion-selective path, I_{membrane}, to cease to zero after 90 s, which corresponds to a vanishing of the fast charge-generating counterion flux to preserve electroneutrality. Subsequently, the current through the nonselective ionic path approaches a steady-state value (8.6 μA, in this case), as the ionic resistance of the cross-channel approaches a specific value determined by the ion concentration pattern. There also exist zero or positive gating voltages that can never be reached by the voltage field in the cross-channel. Shown in the inset of Fig. 2(c), the transmembrane current I_{membrane} does not vanish when the gating voltage V_g is set to 0 V. Hence, the electroneutrality in the system can never be met, resulting in the space-charge generation that can drive charging and discharging events, which are observed in the unstable I_{membrane} after 250 s in the Fig. 2(c) inset.

A series of experimental data correlating the steady-state ionic resistance of the cross-channel with the quasistationary depletion length is shown in Fig. 3 for a constant V_d ($-15\,V$) but a V_g that varies from −0.5 to −3 V. The depletion length L_{dep} is extracted from the fluorescence image when the cross-channel current first reaches the steady-state value. The depletion-amplified ionic resistance $R_{\text{cross-channel}}$ is compared with the original ionic resistance of the cross-channel without any gating effect, which is calculated based on the channel geometry and the initial homogeneous electrolyte condition (Fig. 3), showing the increase of the ionic resistance due to the low mobile-ion concentration within the depletion region. The consistent trend between $R_{\text{cross-channel}}$ and L_{dep} versus V_g clearly confirms that the ionic resistance of the nonselective ionic path is modulated by the gating potential through the specific selection of the depletion length.

Equilibration of V_{membrane} and V_g at steady state allows us to develop a simple scaling theory for the cross-channel resistance. Through ionic current balance $[(V_s - V_g)/R_s] = [(V_g - V_d)/R_d]$, and given that the cross-channel $R_{\text{cross-channel}} = R_s + R_d$, we then have $R_{\text{cross-channel}} = (V_d/V_g)R_s$. We define the length ratio between the distance from the S end to the AEM and the entire cross-channel length as f, so that the ratio between R_s and the original ionic resistance of the cross-channel is also f. Here, we neglect the enrichment effect on the left side of the membrane since, under our voltage relationship, we expect that the enrichment does not affect the ionic resistance as strongly as the depletion in the shared section. We can then normalize the $R_{\text{cross-channel}}$ by the original ionic resistance of the cross-channel without any gating. So the normalized depletion-amplified ionic resistance $\overline{R_{\text{cross-channel}}} = f(V_d/V_g)$. For a given channel design, the amplification of the ionic resistance of the nonselective cross-channel at steady state depends only on the ratio of the applied voltages and the relative position of the ion-selective membrane. The normalized ionic resistance is not influenced by the channel dimension, the electrolyte ionic strength, or the type or strength of the membrane selectivity, which makes this system

versatile for various high-throughput medical applications that operate with complex buffers, large microchannels (up to a few hundred micrometers) and with different ion-selective membranes.

To verify this scaling model, we test seven groups of two-channel chronoamperometry characterization against four different chips, each with different channel sizes and membrane positions, and various potential combinations (Fig. 4). The experimental details can be found in the Supplemental Material [19]. The normalized ionic resistance of the cross-channel is extracted from different chips with various V_d and V_g combinations. After scaling, the large scattered data of these seven groups collapse to the curve predicted by the circuit model, as shown in Fig. 4(b).

The inset of Fig. 4(b) illustrates the simulated ion concentration profile close to the AEM in the cross-channel when $f(V_d/V_g) = 3.43$, by using COMSOL Multiphysics, version 3.5a for the relevant Nernst-Planck equations for symmetric electrolytes. We use the model of Yossifon and Chang [11] for the finite-thickness ion-selective membrane. The simulated transmembrane current at steady state is near zero (approximately 38.6 nA, which is 2 orders of magnitude less than the cross-channel current), and the coexistence of an ion enrichment region on the left of the membrane and an ion depletion region on the right of the membrane can be seen in the simulated concentration profile shown in the inset of Fig. 4(b). The simulated image matches the experimental one shown by the fluorescence image in the inset of Fig. 1(a), validating the proposed mechanism that the rapidly advanced depletion front develops into a slowly evolving one around a quasistationary position to preserve electroneutrality.

IV. CONCLUSIONS

In summary, this paper presents a strategy to establish a quasistable but nonuniform ion concentration distribution in a microfluidic system. By gating a nonselective microfluidic channel with an ion-selective membrane, an ion depletion front is generated from the ion-selective membrane and is subsequently arrested at a quasistationary position in the microfluidic channel due to the global electroneutrality constraint. We can precisely control the position of the quasistationary depletion front and hence select the steady-state ionic resistance of the nonselective microchannel by assigning only an appropriate combination between the external gating voltage V_g and the draining voltage V_d. Because counter bulk flows commonly used to stop the advance of the depletion front are not needed in this approach, we are able to simplify the design of the microfluidic system and to minimize analyte dispersion. A circuit scaling theory based on ionic current balance and the electroneutrality constraint is developed to analyze the control of the depletion-amplified ionic resistance through external voltages. The proposed mechanism to realize a temporally slowly evolving but spatially inhomogeneous ion concentration distribution is robust and insensitive to the channel geometry, ion selectivity, and electrolyte ionic strength of the microfluidic system. Hence, it can be adapted into a wide range of applications with complex buffers and large microchannels. For example, we anticipate that this strategy can lead to an alternative on-chip isotachophoretic sample-pretreatment device for the purification, separation, and concentration of low-mobility biomarkers like nucleic acids and

exosomes. Such a device should prove invaluable in future high-throughput and integrated liquid-biopsy platforms.

ACKNOWLEDGMENTS

We acknowledge the support of NIH Grant No. 1R21AI105361–01A1 and the support of a China Scholarship Council fellowship for Z. P. We would also like to thank Dr. Jarrod Schiffbauer and Professor Zdenek Slouka for the helpful discussions.

References

[1]. Chang H-C and Yeo LY, Electrokinetically Driven Microfluidics and Nanofluidics (Cambridge University Press, Cambridge, England, 2010).

[2]. Levich VG, Physicochemical Hydrodynamics (Prentice-Hall, New York, 1962);Thamida S and Chang H-C, Nonlinear electrokinetic ejection and entrainment due to polarization at nearly insulated wedges, Phys. Fluids 14, 4315 (2002).

[3]. Rubinstein I, Electro-Diffusion of Ions, Vol. 11 (SIAM, Philadelphia, 1990).

[4]. Yariv E and Almog Y, Ionic Currents in the Presence of Supporting Electrolytes, Phys. Rev. Lett. 105, 176101 (2010).

[5]. Ben Y and Chang H-C, Nonlinear Smoluchowski slip velocity and micro-vortex generation, J. Fluid Mech. 461, 229 (2002).

[6]. Yan Y, Wang L, Xue J, and Chang H-C, Ion current rectification inversion in conic nanopores: Nonequilibrium ion transport biased by ion selectivity and spatial asymmetry, J. Chem. Phys. 138, 044706 (2013).

[7]. Hou X, Guo W, and Jiang L, Biomimetic smart nanopores and nanochannels, Chem. Soc. Rev. 40, 2385 (2011). [PubMed: 21308139]

[8]. Sun G, Senapati S, and Chang H-C, High-flux ionic diodes, ionic transistors and ionic amplifiers based on external ion concentration polarization by an ion exchange membrane: A new scalable ionic circuit platform, Lab Chip 16, 1171 (2016); [PubMed: 26960551] Egatz-Gomez A, Wang C, Klacsmann F, Pan Z, Marczak S, Wang Y, Sun G, Senapati S, and Chang H-C, Future microfluidic and nanofluidic modular platforms for nucleic acid liquid biopsy in precision medicine, Biomicrofluidics 10, 032902 (2016);Cheng L-J and Chang H-C, Microscale *pH* regulation by splitting water, Biomicrofluidics 5, 046502 (2011);Switchable *pH* actuators and 3D integrated salt bridges as new strategies for reconfigurable microfluidic free-flow electrophoretic separation, Lab Chip 14, 979 (2014). [PubMed: 24430103]

[9]. Quist J, Janssen KGH, Vulto P, Hankemeier T, and van der Linden HJ, Single-electrolyte isotachophoresis using a nanochannel-induced depletion zone, Anal. Chem. 83, 7910 (2011); [PubMed: 21861489] Quist J, Vulto P, van der Linden H, and Hankemeier T, Tunable ionic mobility filter for depletion zone isotachophoresis, Anal. Chem. 84, 9065 (2012); [PubMed: 23013213] Marczak S, Senapati S, Slouka Z, and Chang H-C, Induced nanoparticle aggregation for short nucleic acid quantification by depletion isotachophoresis, Biosens. Bioelectron. 86, 840 (2016). [PubMed: 27494807]

[10]. Chang H-C, Yossifon G, and Demekhin EA, Nanoscale electrokinetics and microvortices: How microhydrodynamics affects nanofluidic ion flux, Annu. Rev. Fluid Mech. 44, 401 (2012).

[11]. Yossifon G and Chang H-C, Selection of Nonequilibrium Overlimiting Currents: Universal Depletion Layer Formation Dynamics and Vortex Instability, Phys. Rev. Lett. 101, 254501 (2008).

[12]. Zaltzman B and Rubinstein I, Electro-osmotic slip and electroconvective instability, J. Fluid Mech. 579, 173 (2007).

[13]. Kim SJ, Wang Y-C, Lee JH, Jang H, and Han J, Concentration Polarization and Nonlinear Electrokinetic Flow near a Nanofluidic Channel, Phys. Rev. Lett. 99, 044501 (2007).

[14]. Dydek EV, Zaltzman B, Rubinstein I, Deng DS, Mani A, and Bazant MZ, Overlimiting Current in a Microchannel, Phys. Rev. Lett. 107, 118301 (2011).

[15]. Lee JH, Song Y-A, and Han J, Multiplexed proteomic sample preconcentration device using surface-patterned ion-selective membrane, Lab Chip 8, 596 (2008); [PubMed: 18369515] Liu V, Song Y-A, and Han J, Capillary-valve-based fabrication of ion-selective membrane junction for electrokinetic sample preconcentration in PDMS chip, Lab Chip 10, 1485 (2010). [PubMed: 20480116]

[16]. Pu Q, Yun J, Temkin H, and Liu S, Ion-enrichment and ion-depletion effect of nanochannel structures, Nano Lett. 4, 1099 (2004).

[17]. Kim M, Jia M, and Kim T, Ion concentration polarization in a single and open microchannel induced by a surface-patterned perm-selective film, Analyst 138, 1370 (2013); [PubMed: 23293785] Jia M and Kim T, Multiphysics simulation of ion concentration polarization induced by a surface-patterned nanoporous membrane in single channel devices, Anal. Chem. 86, 10365 (2014). [PubMed: 25266500]

[18]. Hunter RJ, Foundations of Colloid Science, Vol. 2 (Clarendon Press, Oxford, 1989).

[19]. See Supplemental Material at 10.1103/PhysRevApplied.7.064024 for experimental details.

[20]. Kirby BJ and Hasselbrink EF, Zeta potential of microfluidic substrates: 2. Data for polymers, Electrophoresis 25, 203 (2004). [PubMed: 14743474]

[21]. Kim SJ, Li LD, and Han J, Amplified electrokinetic response concentration polarization near nanofluidic channel, Langmuir 25, 7759 (2009). [PubMed: 19358584]

[22]. Qu Y, Marshall LA, and Santiago JG, Simultaneous purification and fractionation of nucleic acids and proteins from complex samples using bidirectional isotachophoresis, Anal. Chem. 86, 7264 (2014). [PubMed: 24945850]

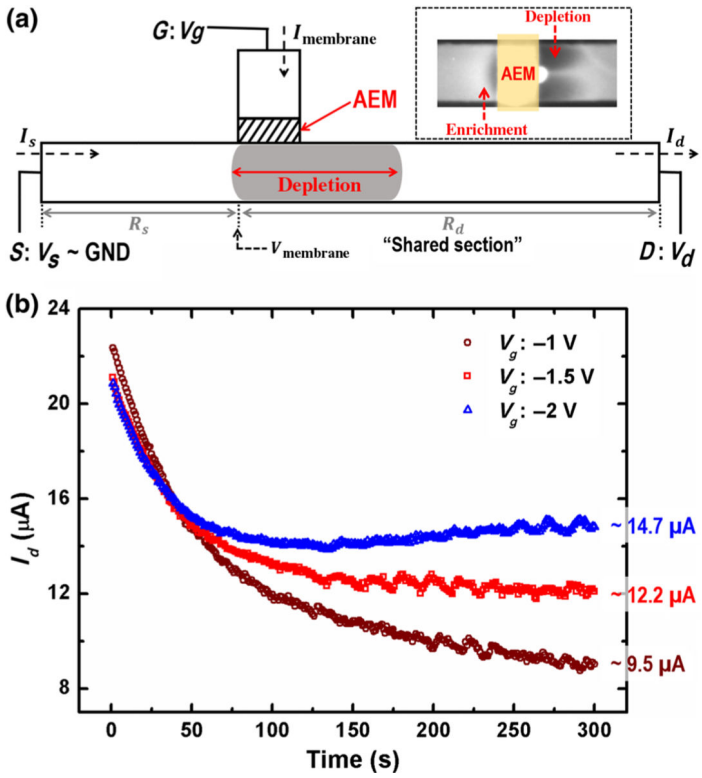

FIG. 1.

(a) Schematic of the hybrid ionic path device. (Inset) Fluorescent imaging of simultaneous ion depletion and enrichment on the same side of the AEM membrane. The image is taken from the bottom of the cross-channel, with $V_d = -15$ V and $V_g = -3$ V. (b) Temporal evolution of cross-channel current I_d with different V_g's (−1, −1.5, and −2 V), approaching a different steady-state current for different V_g's. $V_d = -20$ V in all three experiments.

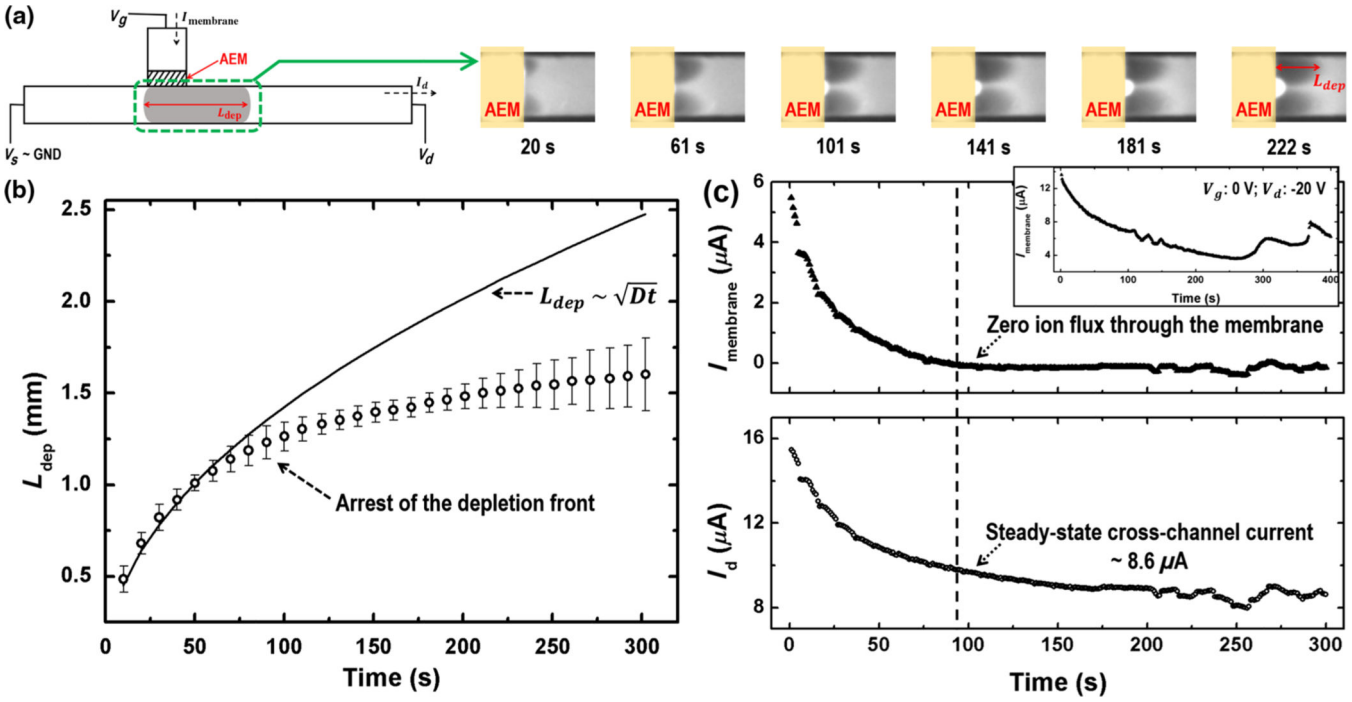

FIG. 2.

(a) Fluorescence images of the depletion front at the indicated times. (b) Time evolution of the instantaneous depletion-region length. Also depicted is the $(\sqrt{Dt})$ scaling as a continuous line. A clear break from the self-similar scaling of the depletion-length growth is observed after 90 s. (c) The charge-generating counterion flux through the AEM (I_{membrane}) decreases to zero after 90 s. Correspondingly, the cross-channel current I_d approaches a steady-state value beyond that time. $V_d = -15$ V and $V_g = -2.5$ V in the experiment. The inset shows that the transmembrane current I_{membrane} becomes unstable at $V_g = 0$ V and $V_d = -20$ V. I_{membrane} cannot vanish to maintain system electroneutrality since the voltage in the cross-channel across the membrane cannot reach the zero gating voltage.

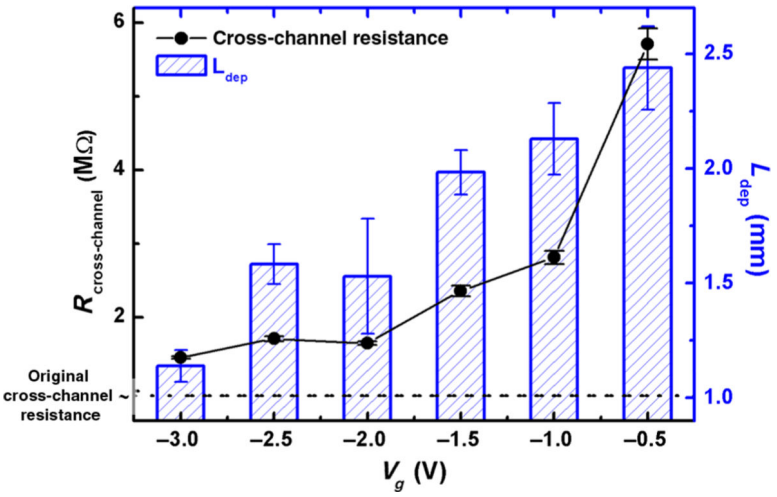

FIG. 3.

The ionic resistance of the cross-channel shows strong correlation with the depletion-region length and the gating voltage V_g. $V_d = -15$ V in all experiments.

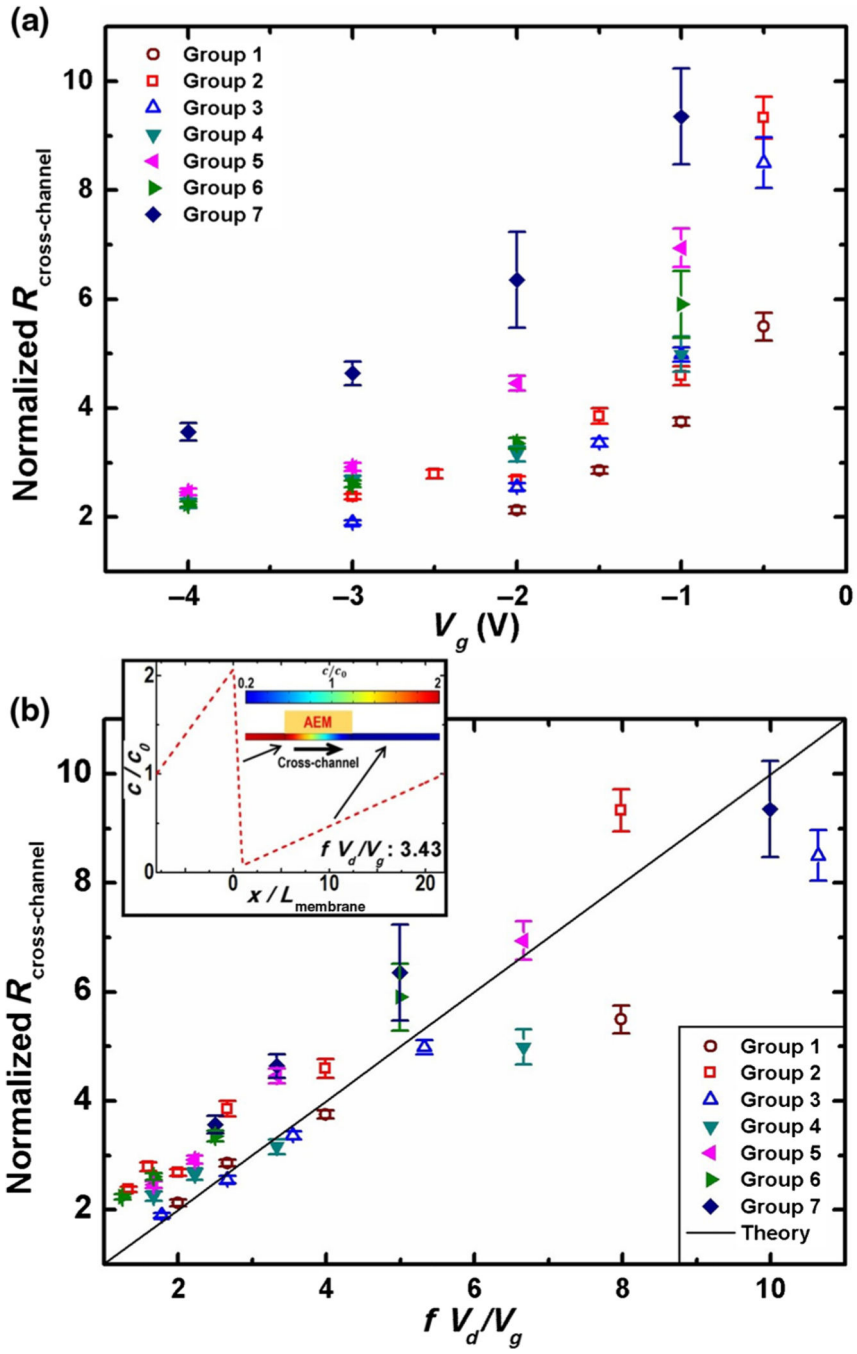

FIG. 4.

(a) The normalized ionic resistance of the cross-channel increases with a higher gating voltage which results in a longer depletion region, regardless of the channel geometry. (b) Collapsed normalized ionic-resistance data by the scaling theory with respect to a normalization factor that contains the gating potential V_g, the draining potential V_d, and the membrane position factor f. The parameter f is defined as the length ratio between the distance from the left end of the cross-channel to the membrane and the entire cross-channel length. (Inset) Simultaneous enrichment and depletion at the vicinity of the membrane in the

cross-channel by simulation, as is consistent with the fluorescent image of Fig. 1(a). Groups 1–7 correspond to four different chip designs with different experimental setups. Detailed experimental information is provided in the Supplemental Material [19].